

In Cooperation with the Edwards Aquifer Authority

Helicopter Electromagnetic and Magnetic Survey Data and Maps, Seco Creek Area, Medina and Uvalde Counties, Texas

By

Bruce D. Smith, David V. Smith, Patricia L. Hill, and Victor F. Labson

This report is preliminary and has not been reviewed for conformity with U.S. Geological Survey editorial standards or with North American Stratigraphic Code.

Any use of trade, product, or firm names is for descriptive purposes only and does not constitute endorsement by the U.S. Government.

Open-File Report 03-226

U.S. DEPARTMENT OF THE INTERIOR

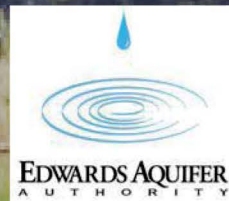


Table of Contents

Abstract.....	ii
Introduction.....	1
Geologic Setting.....	3
Hydrologic Setting.....	6
Helicopter Geophysical Survey.....	6
Apparent Resistivity Maps.....	7
Digital Data.....	9
Conclusions.....	10
Appendix.....	12

Abstract

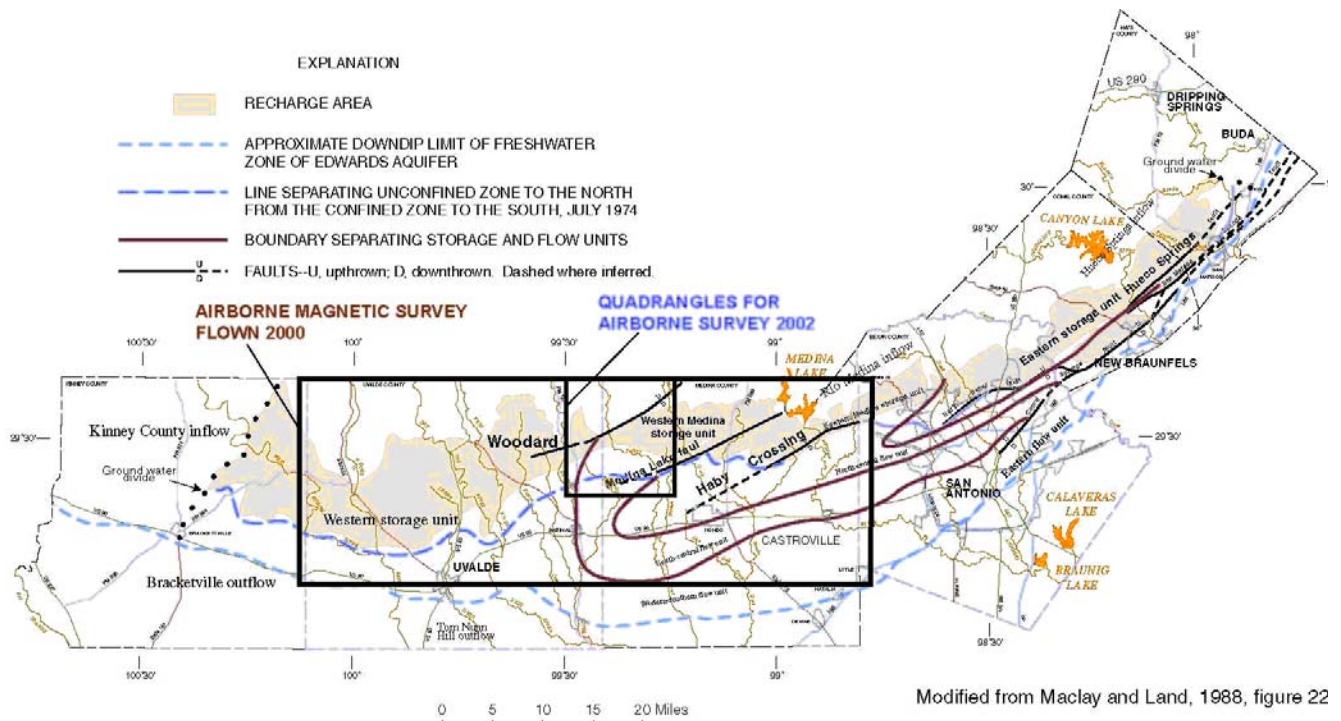
A helicopter electromagnetic and magnetic (HEM) survey was completed of a 209 square kilometer (81 square miles) area of the central Edwards aquifer. This open-file report is a release of the airborne geophysical data and a summary of the hydrologic application. The survey area was centered on the Valdina Farms sinkhole along the Seco Creek drainage in western Medina County, Texas. Flight lines were flown north south with three east west tie lines to aid in leveling the magnetic data. Additional lines were flown on each side of the Seco and Little Seco Creek drainages. A five kilometer (4 mile) extension of 15 lines was flown north of the main survey block centered on Seco Creek. This digital data release contains the flight line data, grids, and maps of the HEM survey data.

The Edwards aquifer in this area consists of three hydrologic zones: catchment, recharge, and confined. The Glen Rose Formation is exposed in the catchment area. The recharge zone is situated in the Balcones fault zone where the Devils River Group of the Edwards aquifer has been exposed by normal faults. The magnetic data is not discussed in depth here, but does have high amplitude closed anomalies caused by shallow igneous intrusives. The Woodard Cave Fault that separates the recharge and catchment zones is in places associated with a weak linear magnetic low.

The HEM data has been processed to produce apparent resistivities for each of the six EM coil pairs and frequencies. Maps of the apparent resistivity for the five horizontal coil pairs show that the catchment, recharge, and confined zones all have numerous linear features that are likely caused by structures, many of which have not been mapped. The distribution of high resistivity areas reflects the lithologic differences within the Trinity and Edwards aquifers.

Introduction

A successful high resolution airborne magnetic survey of the central Edwards and Trinity aquifers (Smith and Pratt, 2003; Smith and others, 2002) set the stage for additional applications of airborne geophysical surveys to hydrologic studies in the area. The U.S. Geological Survey (USGS), as part of a geological, geophysical, and hydrologic study of the Edwards aquifer, funded a helicopter electromagnetic and magnetic (HEM) survey to demonstrate the application to map subsurface features important in understanding and modeling the hydrology of the Edwards and associated aquifers. The Edwards Aquifer Authority funded additional flying to increase the survey area from 93 square kilometers (36 square miles) to 209 square kilometers (81



square miles).

Figure 1 Location of airborne geophysical surveys over the central Edwards Aquifer system.

The Seco Creek watershed was chosen for this detailed study (Figure 1) for a number of reasons:

- 1) the study area encompassed a typical stratigraphic section including the catchment, recharge, and confined areas,
- 2) the survey area covered a north-south section of the Balcones Fault Zone containing a variety of structural styles,
- 3) one of the most prominent recharge and diversion features, the Valdina Farms Sinkhole, is located in the central part of the survey area, and
- 4) several USGS and Texas Bureau of Economic Geology (BEG) studies covered the area and are currently active.

The HEM survey used the RESOLVE[®] system flown by Fugro Airborne Surveys, which uses five horizontal coplanar coils and one vertical coaxial coil. The specific frequencies are given in Table 1. The system also includes in the bird (sensor housing) a total field magnetometer, differential kinematic GPS, and laser altimeter. The helicopter carries another differential GPS system, barometric and radar altimeters, and a video camera. Electromagnetic noise from power lines and natural sources (lightning) are also measured. The survey was flown with north-south flight lines and a nominal line spacing of 200 m with a sensor elevation of 30 m except as required for safety considerations and FAA regulations. The system was calibrated before and after the survey on the ground in the central part of the survey area away from power lines and other cultural noise. System calibration was also checked at the Fugro Airborne offices in Toronto when the system returned. In addition four lines were flown along the Seco and Little Seco Creeks. These flight lines were flown to provide data directly along the drainages with consistent flight elevation and time (flight number).

Table 1 Frequencies and sensitivities for the HEM survey.

COIL CONFIGURATION	FREQUENCY (Hz)	SENSITIVITY (ppm)
Coplanar	386	0.13
Coplanar	1514	0.12
Coaxial	3315	0.06
Coplanar	6122	0.24
Coplanar	25960	0.44
Coplanar	106400	0.44

Geologic Setting

Sedimentary rocks of the Seco Creek watershed are given in the stratigraphic section shown in Figure 2 and are described in detail by Maclay (1995) and Small and Clark (2000). The oldest, lower Cretaceous, rocks are the upper and lower members of the Glen Rose Limestone which is part of the Trinity Group. An evaporate unit is found at the base of the upper member. These units have a thickness greater than 150 m (500 ft). Mapping in the area by the Texas Bureau of Economic Geology (Murray and Collins, 2003) has not subdivided the Glen Rose Limestone. The Devils River is divided into upper and lower parts in this stratigraphic section (Figure 2) and are equivalent to the Segovia Formation (lower Devils River) and Fort Terrett Formation (upper Devils River) as described by Rose (1972). Small and Clark (2000) do not divide the Devils River in this area. The upper Devils River is more cavernous. The Georgetown formation at the top of the late Cretaceous section is rather impervious limestone and marl.

The upper Cretaceous consists of several formations (Figure 2) including (from oldest to youngest) the Del Rio Clay, Buda Limestone, Eagle Ford Group, Austin Group, Anachacho Limestone, and Escondido Formation. The Del Rio Clay is approximately 15 m (50 ft) thick. The Austin Group is massive chalk to marly flaggy limestone. The Eagle Ford is about 22 m (70 ft) and contains black shales. All of these units have a higher electrical conductivity than the more massive limestones of the Edwards and Trinity Groups. This high conductivity of the Del Rio Clay is used in electrical logs as a stratigraphic marker.

The Tertiary formations consist of the Midway and Wilcox Groups which together range in thickness from 200 to 500 feet thick. These units consist of shales, sandstones, siltstones, and some limestone. The Uvalde and Leona gravels overlay these units and are less than 100 feet thick.

The Balcones fault zone is the major structural feature of the study area. Uplift of the Edwards Plateau in the Miocene and subsidence of the Gulf of Mexico created a zone of normal faults. This zone is defined by a number of northeast trending faults (Figure 3) and is the southern end of the Edwards plateau. Some cross faults trend northwest to southeast. Most of the faults are normal with the downthrown side to the southeast toward the Gulf of Mexico. The Woodard Cave fault is the contact between the Trinity and Edwards Groups (Figure 3) in the Seco Creek area. It has a maximum displacement of about 600 feet. Many of the faults are more like fracture or shatter zones rather than sharp breaks. Some faults have gouge and small boulders.

LIST OF MAP UNITS

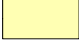
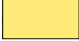












	Qal, Alluvium	
	Qu, undivided terrace, slope-wash deposits, and fan deposits	
	Qt, Terrace deposits	
	Qle, Leona Formation	
	QTu, Uvalde gravel (older alluvium)	
	Ki - Intrusive igneous rocks	
	Kes - Escondido Formation	
	Kan, Anacacho Formation	
	Kan+Kau, Anacacho Formation + Austin Group	
	Kau, Austin Group	
	Kef, Eagle Ford Formation	
	Kbu, Buda Formation	
	Kdr, Del Rio Formation	
Edwards Group		
	Kdvru, upper Devils River Formation	
	Kdvrl, lower Devils River Formation	 Kft, Fort Terrett Formation
Trinity Group		
	Kgru, upper Glen Rose Formation	

Figure 2 Stratigraphic section for the Seco Creek area (Murray and Collins, 2003).

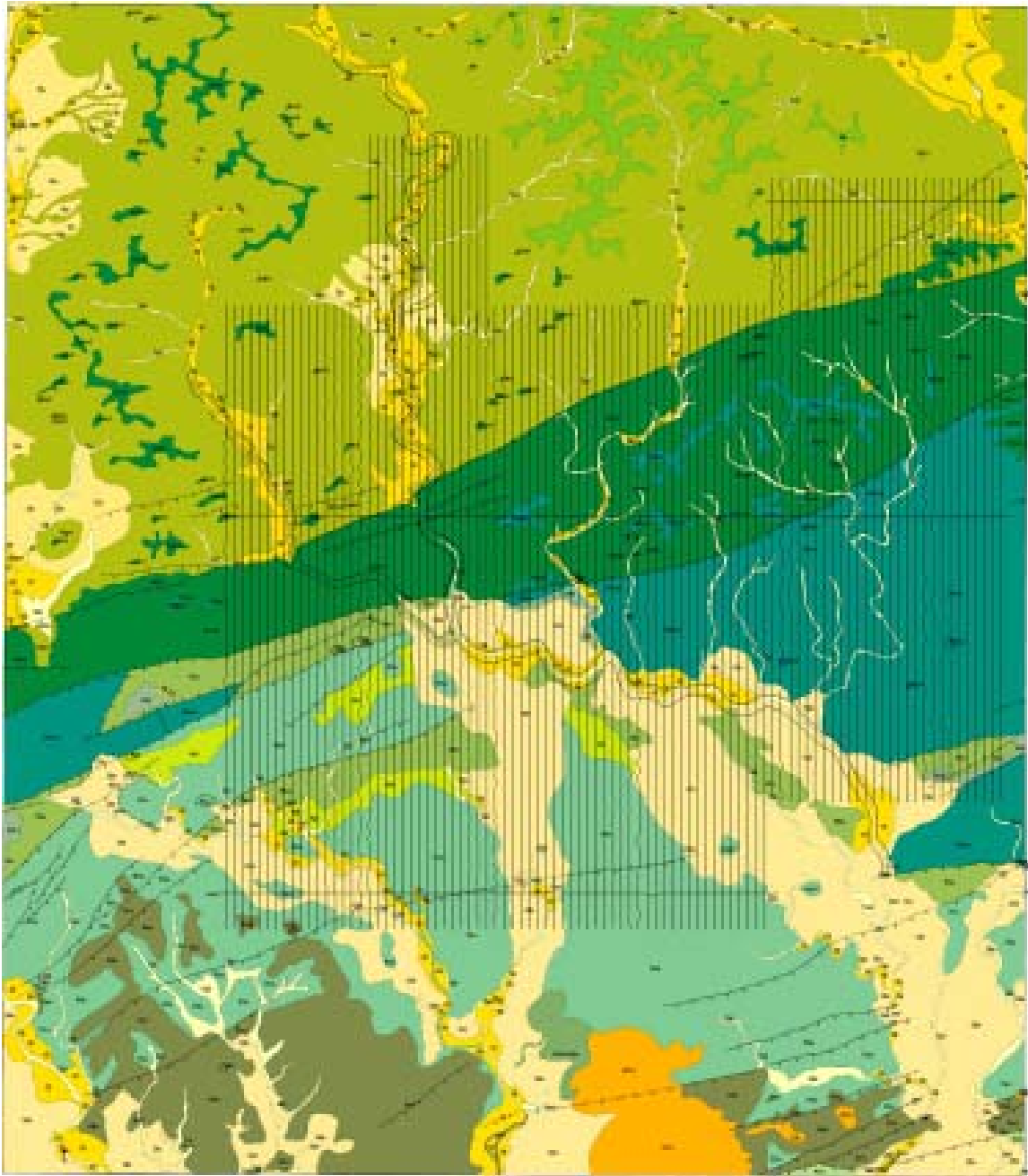


Figure 3. Geologic map (Murray and Collins, 2003) of the four 7.5 minute quadrangles in the upper Seco Creek Watershed. Lithologic units are given in Figure 2. North-South lines are the flight path for the HEM survey. Black lines are faults (dashed where inferred). Seco Creek occupies the yellow Quaternary areas in the central part of the survey area.

Hydrologic Setting

The Trinity Group in the northwest part of the survey area is termed the catchment zone since drainages cross this zone with presumed little recharge to the Edwards Aquifer. The Trinity Group is much less permeable than the Edwards Group but is locally cavernous. For example during normal flow, Seco Creek flow disappears in sink holes just north of the fault contact with the Edwards. There have been no studies of possible interconnection of recharge paths between the Trinity and Edwards in this area. However the relatively lower permeability due to shales and marls of the Trinity makes it a lower confining unit for the Edwards.

The Edwards Group exposed by the normal Balcones fault zone in the central part of the survey area (Figure 3) is termed the recharge zone. This part of the aquifer has a very high porosity and permeability typical of a karstic terrain developed since the Miocene uplift. Lithology, stratigraphy, diagenesis, and selective dissolution (karstification) account for the effective porosity and permeability of the aquifer. Cave development is controlled by both lithology and structure.

In addition to the Trinity and Edwards aquifers, the Leona and Uvalde gravels constitute the other aquifers in the area. These aquifers have not been studied in the same detail as the Trinity and Edwards.

Faults in the area may act to increase the permeability by causing the development of fractures. Development of fault gouge may increase the clay content of the fault zones and effectively reduce the permeability. Clay zones could actually be aquitards impeding local groundwater flow.

Helicopter Geophysical Survey

Both electromagnetic and magnetic field measurements were made over the survey area. Smith and Pratt (2003) briefly discuss magnetic data for the survey area in the context of the larger high resolution aeromagnetic survey of the central Edwards Aquifer. The main conclusion at this stage of processing of the magnetic data is that a linear slight magnetic low can be correlated with parts of the main Woodard Cave fault. Additional processing of the magnetic data and ground follow up surveys are needed before any interpretation of this magnetic feature can be made. There appears to be no magnetic anomalies associated with the numerous other structures. A Cretaceous age intrusive is marked by a magnetic high in the northwest part of the survey (Figure 8 in Smith and Pratt, 2003). There are no indications of igneous dikes

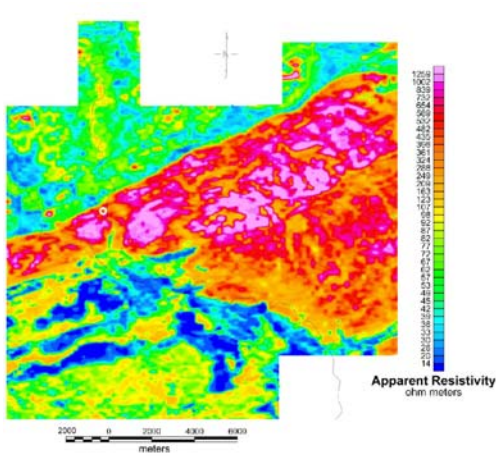
in this relatively high resolution magnetic survey. Data processing at this point has concentrated on the electromagnetic field measurements and is described below.

Apparent Resistivity Maps

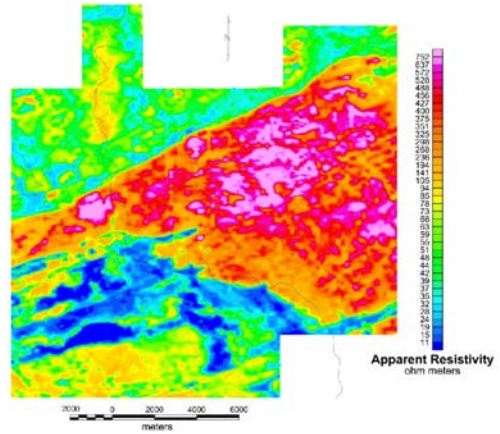
Apparent resistivity is the resistivity of a homogeneous isotropic volume that would give the same electromagnetic signal as measured by the HEM system. Fugro Airborne as part of the contracted data processing has computed the apparent resistivity for each frequency. The computation is based on the pseudo-layer model (Fraser, 1978). Yin and Hodges (2003) discuss this method of apparent resistivity calculation and utilize it in an analysis of electrical anisotropy for this survey. Figure 4 shows apparent resistivity maps for the five horizontal coplanar coil frequencies (Table 1). The color scale has the same stretch between the highest and lowest measured apparent resistivity for each map. The highest apparent resistivity decreases an order of magnitude as frequency decreases 1.5 orders of magnitude (see figure caption), from 1300 to 150 ohm meters. The color scales have been used to emphasize comparative high and low resistivity areas within each map (at each frequency) rather than between maps. Note also that a resistivity color scale is used so that high resistivity (low conductivities) areas are in the warmer colors (reds) and areas of low resistivities (high conductivities) in the cooler colors (blues).

In general each map in Figure 4 shows progressively (from 4a to 4e) deeper sections of the earth. Smith and others (2003) discuss specific variations based on preliminary resistivity depth sections. Each part of the Edwards aquifer system is characterized by contrasting apparent resistivities. The lowest apparent resistivities are associated with the confining units in the southwest quadrant of the survey. The thick Del Rio Clay is source of the low resistivities. The electrically resistive Buda Limestone, stratigraphically above the clay, is found in higher elevations. Gravels along the drainages are also more resistive than many of the older confining layers.

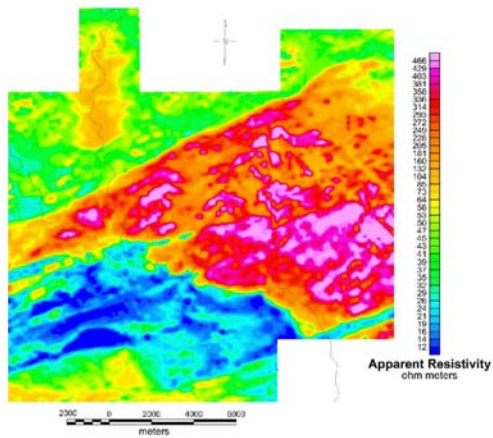
The central northwest trending highest resistivities are from the exposed parts of the Devils River. The high resistivities at 100 and 25 kHz (Figure 4a and 4b) suggest a difference within the Devils River that correlates with the upper and lower divisions shown in Figure 4. The geophysical maps show more detail and precise locations than the geologic map. Lower apparent resistivities in the area of the lower Devils River at 400 Hz (northern part of the catchment zone) suggest that the more conductive upper Glen Rose influences these apparent resistivities.



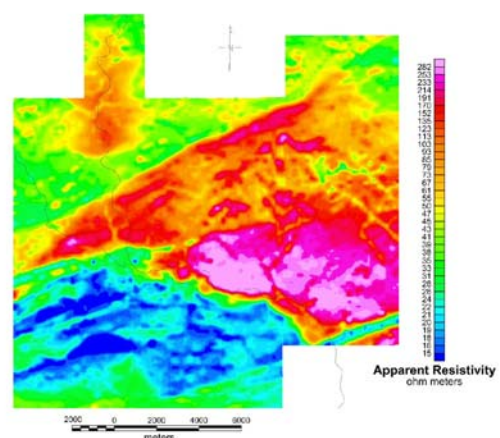
a. 100 KHz



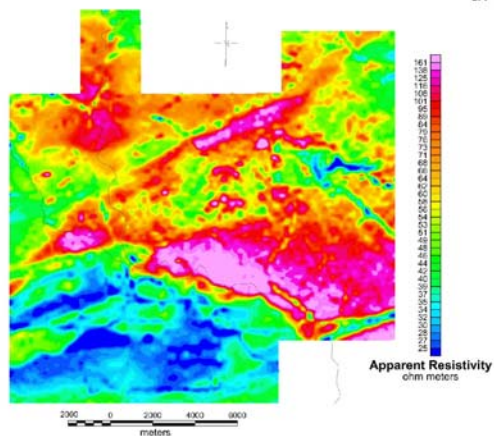
b. 25 KHz



c. 6200 Hz



d. 1500 Hz



e. 400 Hz

Figure 4. Apparent resistivity maps for each horizontal coplanar coil pair. High resistivities (warm colors) for each frequency are (rounded up): a. 1300, b. 800, c. 500,

d. 300, e. 150 ohm meters. The distance scale is 4 km or 2.5 miles (see also Plate 1).

Moderate resistivities in the northwest part of the survey area can be attributed to the Glen Rose Formation. The upper Glen Rose just north of the Woodard Cave fault maybe somewhat more conductive than the lower unit further to the north. The upper and lower Glen Rose appear to be in fault contact. There is an interesting but unexplained area of high resistivity in the upper Glen Rose along the northern part of Seco Creek (the northern extension of the central part of the survey area). The higher resistivity could be due to a more resistive limestone lithology at depth.

Linear apparent resistivity features correlate with known structures and suggest structures that have not been mapped. The narrow low resistivity trough in the southeast corner of the survey area (Figure 4) generally corresponds to a mapped graben (Figure 3) in the same area but can be much better defined from the geophysical maps since the graben structure is not exposed. The northeast trending structure that causes this graben, correlates with linear features in the confined zone to the west suggesting it extends further to the west than mapped. Other narrow zones in the confining units are suggestive of other similar structures that are covered. High resistivity linear features in the Edwards recharge area suggest structures along which there may be increased permeability due to fracturing or karstification.

Digital Data

Flight line data is given in an ASCII database in the directory [linedata](#). The position is given in latitude and longitude as well as UTM coordinates. The raw GPS positioning data for the survey is in NAD83 (zone 14N) but has been reprocessed to NAD27 (zone 14N) in the database. The header for each channel is given in the txt file in the directory. Each channel is described in the contractors report given in the appendix and the [reports](#) directory.

Grids of the magnetic field data and the apparent resistivities for the horizontal coplanar coil pairs are given in the [grids](#) directory. The apparent resistivities have been corrected for system drift and calibrations as described in the contractor's report (appendix and [reports](#) directory). The grid cell size is 50 m. This is large in comparison to the measurement spacing along flight lines (about 3 m) because the spacing between flight lines is larger than the measurement interval. The grids are in grid exchange format ([Grids\gxf_grid_documentation.pdf](#)), a "standard" of the geophysical industry used in many map display programs.

The directory [MapImages](#) contains geotiff (UTM projected tif files) of the grids. Each file has an associated world file (tfw). In addition this directory contains AutoCad format files (extension dxf) of the flight lines. These files are also

georeferenced to the NAD27 projection. Plate 1 shows plots of the map images.

Conclusions

The HEM survey of the Seco Creek area has mapped both the magnetic and electrical characteristics of geologic and hydrologic features from the near surface to depths on the order of 100 m. The magnetic survey data has not been discussed in detail here but does show some anomalies possibly associated with structures and a few high amplitude anomalies related to igneous intrusives. The HEM data has been processed to produce apparent resistivity maps. These maps show that the catchment, recharge, and confined zones all have numerous linear features that reflect exposed and covered structures. These structures are important in understanding and modeling the hydrology of each zone. There are areas of relatively high resistivity in the catchment and recharge zones that reflect lithologic differences perhaps related to stratigraphic changes.

References

- Elliott, W.R. and Veni, G., 1994, The Caves and Karsts of Texas: National Speleological Society Convention Guidebook, 342 p.
- Haung, H. and Fraser, D.C., 1996, The differential parameter method for multifrequency airborne resistivity mapping: *Geophysics*, vol. 61, p. 100-109.
- Fraser, D.C., 1978, Resistivity Mapping with an Airborne Multicoil Electromagnetic System: *Geophysics*, vol. 43, p. 144-172.
- Maclay, R.W., 1995, Geology and Hydrology of the Edwards Aquifer in the San Antonio Area, Texas: U.S. Geological Survey Water Resources Investigations Report 95-4186, 64p.
- Murray, K.E. and Collins, E.W., 2003, GIS Compilation of Geologic Map Data for the Seco Creek Area, Medina County, Texas: U.S. Geological Survey, Open File Report, in preparation.
- Small, T.A. and Clark, A.K., 2000, Geologic Framework and Hydrogeologic Characteristics of the Edwards Aquifer Outcrop, Medina County Texas: U.S. Geological Survey Water Resources Investigations Report 00-4195.

- Smith, B.D., Irvine, R., Blome, C., Clark, A.K., and Smith, D.V., 2003, Preliminary Results, Helicopter Electromagnetic and Magnetic Survey of the Seco Creek Area, Medina and Uvalde Counties, Texas: Proceedings from the Symposium on the Application of Geophysics to Engineering and Environmental Problems, Environmental and Engineering Society, 15p.
- Smith, D.V. and Pratt, D., 2003, Advanced Processing and Interpretation of the High Resolution Aeromagnetic Survey Data over the Central Edwards Aquifer, Texas: Proceedings from the Symposium on the Application of Geophysics to Engineering and Environmental Problems, Environmental and Engineering Society, 11p.
- Smith, D.V., Smith, B.D., and Hill, P.L., 2002, Aeromagnetic Survey of Medina and Uvalde Counties, Texas: A Web Site for Distribution of Data, OFR-02-0049.
- U. S. Geological Survey, 1999, Geologic Framework and Hydrologic Properties of the Seco Creek Watershed, Texas, Fact Sheet FS-104-98, 4 p.
- Yin, C. and Hodges, G., Identification of Electrical Anisotropy from Helicopter EM Data, Proceedings from the Symposium on the Application of Geophysical methods Engineering and Environmental Problems, Environmental and Engineering Society, 12p.

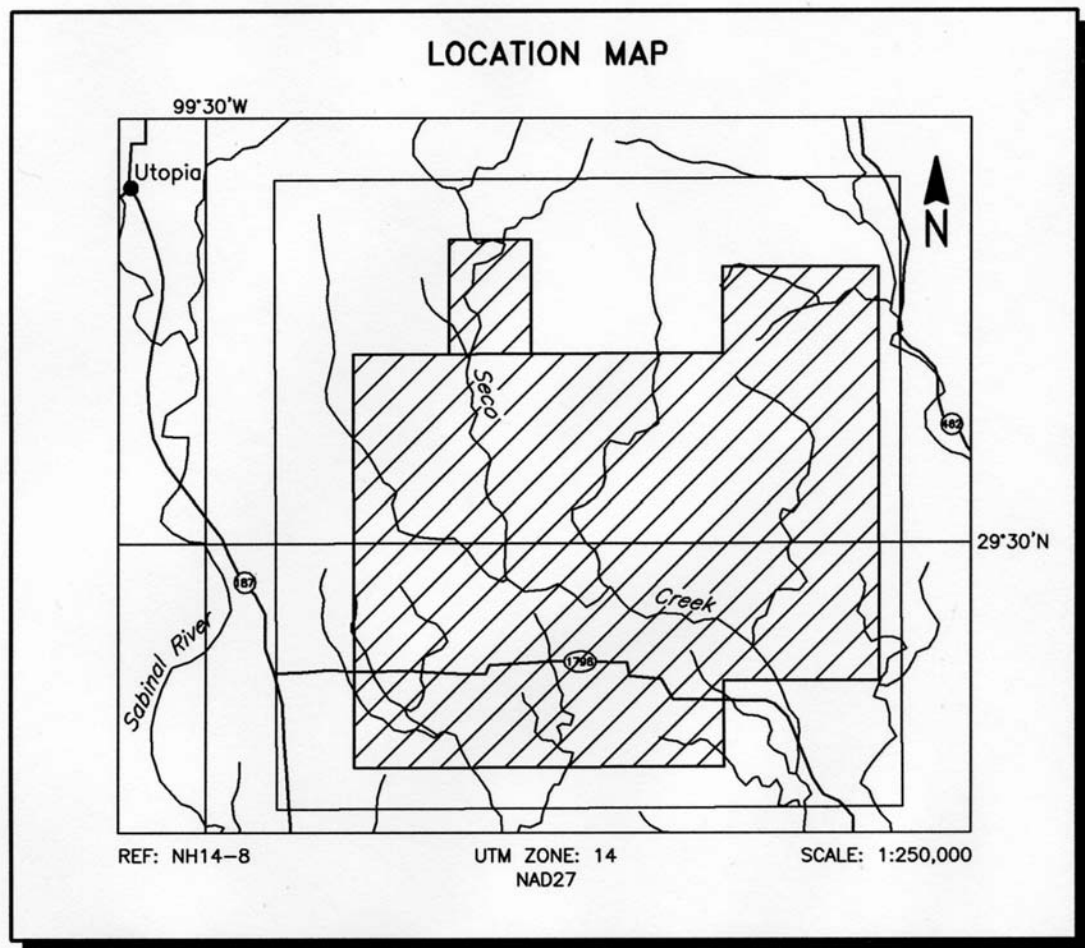


Figure 1.1 Seco Creek area, Texas.

2.0 SURVEY EQUIPMENT AND PROCEDURES

This section provides a brief description of the geophysical instruments, quality control and calibration procedures used to acquire the survey data.

2.1 Electromagnetic System

Model: RESOLVE

Type: Towed bird, symmetric dipole configuration operated at a nominal survey altitude of 98 feet (30 metres). Coil separation is 7.9 metres for 400 Hz, 1500 Hz, 6200 Hz, 25,000 Hz and 100,000 Hz and 9.0 metres for the 3300 Hz coil-pair.

Coil orientations/frequencies:	<u>orientation</u>	<u>nominal</u>	<u>actual</u>
	coplanar	400 Hz	386 Hz
	coplanar	1 500 Hz	1 514 Hz
	coaxial	3 300 Hz	3 315 Hz
	coplanar	6 200 Hz	6 122 Hz
	coplanar	25 000 Hz	25 960 Hz
	coplanar	100 000 Hz	106 400 Hz

Channels recorded: 6 in-phase channels
6 quadrature channels
2 monitor channels

Sensitivity: 0.13 ppm at 400 Hz CP
0.12 ppm at 1 500 Hz CP
0.06 ppm at 3 300 Hz CX
0.24 ppm at 6 200 Hz CP
0.44 ppm at 25 000 Hz CP
0.44 ppm at 100 000 Hz CP

Sample rate: 10 per second, equivalent to 1 sample every 3.5 m, at a survey speed of 125 km/h.

2.2

The electromagnetic system utilizes a multi-coil coaxial/coplanar technique to energize conductors in different directions. The coaxial coil is vertical with its axis in the flight direction. The coplanar coils are horizontal. The secondary fields are sensed simultaneously by means of receiver coils which are maximally coupled to their respective transmitter coils. The system yields an in-phase and a quadrature channel from each transmitter-receiver coil-pair.

Calibration of the system during the survey uses the Fugro AutoCal automatic, internal calibration process. At the beginning and end of each flight, and at intervals during the flight, the system is flown up to high altitude to remove it from any “ground effect” (response from the earth). Any remaining signal from the receiver coils (base level) is measured as the zero level, and removed from the data collected until the time of the next calibration. Following the zero level setting, internal calibration coils, for which the response phase and amplitude have been determined at the factory, are automatically triggered – one for each frequency. The on-time of the coils is sufficient to determine an accurate response through any ambient noise. The receiver response to each calibration coil “event” is compared to the expected response (from the factory calibration) for both phase angle and amplitude, and the applied phase and gain corrections adjusted to bring the data to the correct value.

2.3

In addition, the output of the transmitter coils are continuously monitored during the survey, and the applied gains adjusted to correct for any change in transmitter output (due to heating, etc.)

Because the internal calibration coils are calibrated at the factory (on a resistive halfspace) ground calibrations using external calibration coils on-site are not necessary for system calibration. A check calibration may be carried out on-site to ensure all systems are working correctly. All system calibrations will be carried out in the air, at sufficient altitude that there will be no measurable response from the ground.

The internal calibration coils are rigidly positioned and mounted in the system relative to the transmitter and receiver coils. In addition, when the internal calibration coils are calibrated at the factory, a rigid jig is employed to ensure accurate response from the external coils.

Using real time Fast Fourier Transforms and the calibration procedures outlined above, the data will be processed in real time from measured total field at a high sampling rate to in-phase and quadrature values at 10 samples per second.

2.2 Magnetometer

Model:	Fugro AM102 processor with Geometrics G822 sensor
Type:	Optically pumped cesium vapour
Sensitivity:	0.01 nT
Sample rate:	10 per second

The magnetometer sensor is housed in the EM bird, 29 m below the helicopter.

2.3 Magnetic Base Station

Model:	Fugro CF1
Type:	Digital recording proton precession
Sensitivity:	0.10 nT
Sample rate:	1 second intervals

The base station was located in a magnetically quiet area away from cultural interference. The clock on the base station was synchronized with the airborne magnetometer to UTC time, permitting subsequent removal of the diurnal variation. The magnetic base station was located at approximately WGS84 latitude 29°21.87'N and longitude 99° 9.92'W.

2.4 Radar Altimeter

Manufacturer:	Honeywell/Sperry
Model:	AA 330
Type:	Short pulse modulation, 4.3 GHz
Sensitivity:	0.3 m

The radar altimeter measures the vertical distance between the helicopter and the ground.

This information is used in the processing algorithm that determines conductor depth.

2.5 Analog Recorder

Manufacturer:	RMS Instruments
Type:	DGR33 dot-matrix graphics recorder
Resolution:	4x4 dots/mm
Speed:	1.5 mm/sec

The analog profiles are recorded on chart paper in the aircraft during the survey. Table

2-1 lists the geophysical data channels and the vertical scale of each profile.

2.6

Channel Name	Parameter	Scale units/mm
400I	coaxial in-phase (400 Hz)	5 ppm
400Q	coaxial quad (400 Hz)	5 ppm
1K5I	coplanar in-phase (1500 Hz)	5 ppm
1K5Q	coplanar quad (1500 Hz)	5 ppm
6K2I	coplanar in-phase (6200 Hz)	10 ppm
6K2Q	coplanar quad (6200 Hz)	10 ppm
1X8I	coaxial in-phase (3300 Hz)	10 ppm
1X8Q	coaxial quad (3300 Hz)	10 ppm
25KI	coplanar in-phase (25000 Hz)	20 ppm
25KQ	coplanar quad (25000 Hz)	20 ppm
100I	coplanar in-phase (100000 Hz)	20 ppm
100Q	coplanar quad (100000 Hz)	20 ppm
ALTL	altimeter (laser)	3 m
ALTR	altimeter (radar)	3 m
MAGC	magnetics, coarse	20 nT
MAGF	magnetics, fine	2.0 nT
2SP	coplanar spherics monitor	
2PL	coplanar power line monitor	
1KPA	altimeter (barometric)	30 m
2TDC	internal (console) temperature	1° C
3TDC	external temperature	1° C

Table 2.1 The Analog Profiles, RESOLVE System

2.6 Digital Data Acquisition System

Manufacturer: RMS Instruments

Model: DGR 33

Recorder: SanDisk 48-64 Mb flash cards

2.7

The data are stored on PCMCIA flash cards and are transferred to the field workstation PC at the survey base for verification, backup and preparation of in-field products.

2.7 Video Flight Path Recording System

Type: VHS Colour Video Camera (NTSC)

Model: AG 2400/WVCD132

Fiducial numbers are recorded continuously and are displayed on the margin of each image. This procedure ensures accurate correlation of analog and digital data with respect to visible features on the ground.

2.8 Navigation (Global Positioning System)

Airborne Receiver for Navigation

Model: Ashtech Glonass GG24

Type: SPS (L1 band), 24-channel, C/A code at 1575.42 MHz,
S code at 0.5625 MHz, Real-time differential.

Sensitivity: -132 dBm, 0.5 second update

Accuracy: Manufacturer's stated accuracy is better than 10 metres
real-time

Airborne Receiver for Processing

Model: Ashtech Z-Surveyor

2.8

Type:	Code and carrier tracking of L1 band, 12-channel, dual-frequency C/A code at 1575.42 MHz, and L2 P-code at 1227 MHz
Sensitivity:	0.5 second update
Accuracy:	Manufacturer's stated accuracy for differential corrected GPS is better than 1 metre

Base Station

Model:	Ashtech Z-Surveyor
Type:	Code and carrier tracking of L1 band, 12-channel, dual-frequency C/A code at 1575.42 MHz, and L2 P-code at 1227 MHz
Sensitivity:	0.5 second update
Accuracy:	Manufacturer's stated accuracy for differential corrected GPS is better than 1 metre

The Ashtech GG24 is a line of sight, satellite navigation system which utilizes time-coded signals from at least four of forty-eight available satellites. Both Russian GLONASS and American NAVSTAR satellite constellations are used to calculate the position and to provide real time guidance to the helicopter. The Ashtech system can be combined with a RACAL or similar GPS receiver which further improves the accuracy of the flying and subsequent flight path recovery to better than 5 metres. The differential corrections, which are obtained from a network of virtual reference stations, are transmitted to the helicopter via a spot-beam satellite. For flight path processing an Ashtech Z-surveyor was used as the mobile receiver and base station receiver. The

2.9

mobile and base station raw XYZ data are recorded, thereby permitting post-survey processing for theoretical accuracies of better than 5 metres. The final navigation channels were produced from the Ashtech Z-Surveyor GPS unit which was located on the EM sensor.

The GPS base station was run for a period of at least 24 hours to obtain a master position for post processing. For the Seco Creek survey the GPS station was located at latitude 29° 21' 53.5493"N, longitude 99° 09' 55.2231"W at an elevation of 277.5 metres a.m.s.l. The GPS records data relative to the WGS84 ellipsoid, which is the basis of the revised North American Datum (NAD83).

2.9 Field Workstation and Data Verification

A laptop computer is used at the survey base to verify data quality and completeness. Flight data are transferred to the PC hard drive to permit the creation of a Geosoft database. This process allows the geophysicist to display both the positional and geophysical data on a screen or printer.

3.0 PRODUCTS AND PROCESSING TECHNIQUES

3.1 Base Maps

Base maps of the survey areas are produced from published topographic maps. These provide a relatively accurate, distortion-free base which facilitates correlation of the navigation data to the UTM grid. The original topographic maps are scanned to a digital format and combined with geophysical data for plotting the final maps. All maps are created using the following parameters:

Projection Description:

Datum:	NAD27
Ellipsoid:	Clarke 1866
Projection:	UTM (Zone: 14)
Central Meridian:	99° West
False Northing:	0
False Easting:	500000
Scale Factor:	0.9996
WGS84 to Local Conversion:	Molodensky
X,Y,Z Datum Shifts:	8 -159 -175

Table 3.1 Survey Products

Digital Geosoft GDB archive format on CD-ROM (2 copies)
 Digital grid archives in Geosoft GRD format on CD-ROM (2 copies)
 Survey report (2 copies)
 Analog chart records
 Flight path videocassettes (VHS format)

Note: Other products can be produced from existing survey data, if requested.

3.2 Apparent Resistivity

The apparent resistivity in ohm-metres (ohm-m) can be generated from the in-phase and quadrature EM components for any of the frequencies, using a pseudo-layer half-space model. Resistivity maps portray all the EM information for that frequency over the entire survey area. This contrasts with discrete electromagnetic anomaly maps which provide information only over interpreted conductors. The large dynamic range makes the resistivity parameter an excellent mapping tool.

The preliminary resistivity maps and images are carefully inspected to locate any lines or line segments which might require levelling adjustments. Subtle changes between in-flight calibrations of the system can result in line to line differences, particularly in resistive (low signal amplitude) areas. If required, manual levelling is carried out to eliminate or minimize resistivity differences which can be caused by changes in

3.3

operating temperatures. These levelling adjustments are usually very subtle, and do not result in the degradation of anomalies from valid bedrock sources.

After the manual levelling process is complete, revised resistivity grids are created. The resulting grids can be subjected to a microlevelling filter in order to smooth the data for contouring. The coplanar resistivity parameter has a broad 'footprint' which requires very little filtering.

The apparent resistivities have been calculated for all five coplanar frequencies and the coaxial frequency using the pseudo-layer half-space model. Digital data are contained on the CD-ROM archives. Values are in ohm-m on all final products.

3.3 EM Magnetite (optional)

The apparent percent magnetite by weight is computed wherever magnetite produces a negative in-phase EM response. This calculation is more meaningful in resistive areas, and is not recommended for these survey areas due to the moderately conductive, non-magnetic background and sources of cultural interference.

3.4 Total Magnetic Field

The aeromagnetic data are corrected for diurnal variation using the magnetic base station data. Manual adjustments are applied to any lines that require levelling, as indicated by shadowed images of the gridded magnetic data or tie line/traverse line intercepts. The IGRF gradient is removed from the corrected total field data.

3.5 Calculated Vertical Magnetic Gradient (optional)

The diurnally corrected total magnetic field data are subjected to a processing algorithm which enhances the response of magnetic bodies in the upper 500 m and attenuates the response of deeper bodies. The resulting vertical gradient map provides better definition and resolution of near-surface magnetic units. It also identifies weak magnetic features which may not be evident on the total field map. However, regional magnetic variations and changes in lithology may be better defined on the total magnetic field map.

3.6 Magnetic Derivatives (optional)

The total magnetic field data can be subjected to a variety of filtering techniques to yield maps of the following:

- enhanced magnetics
- second vertical derivative
- reduction to the pole/equator
- magnetic susceptibility with reduction to the pole
- upward/downward continuations
- analytic signal

All of these filtering techniques improve the recognition of near-surface magnetic bodies, with the exception of upward continuation. Any of these parameters can be produced on request.

3.7 Multi-channel Stacked Profiles (optional)

Distance-based profiles of the digitally recorded geophysical data can be generated and plotted by computer. These profiles also contain the calculated parameters that are used in the interpretation process.

3.8 Contour, Colour and Shadow Map Displays

The geophysical data were interpolated onto a regular grid using a modified Akima spline technique. The resulting grid is suitable for generating contour maps of excellent quality. The grid cell size used was 50 metres or 1/4 of the line interval.

Colour maps are produced by interpolating the grid down to the pixel size. The parameter is then incremented with respect to specific amplitude ranges to provide colour "contour" maps.

3.9 Resistivity-depth Sections (optional)

The apparent resistivities for all frequencies can be displayed simultaneously as coloured resistivity-depth sections. The sections can be plotted using the topographic elevation profile as the surface. The digital terrain values, in metres a.m.s.l., are calculated from the GPS Z-value minus the aircraft radar altimeter.

Resistivity-depth sections can be generated in three formats:

3.7

- (1) Sengpiel resistivity sections, where the apparent resistivity for each frequency is plotted at the depth of the centroid of the in-phase current flow¹; and,
- (2) Differential resistivity sections, where the differential resistivity is plotted at the differential depth².
- (3) Occam³ or Multi-layer⁴ inversion.

Both the Sengpiel and differential methods are derived from the pseudo-layer half-space model. Both yield a coloured resistivity-depth section which attempts to portray a smoothed approximation of the true resistivity distribution with depth. Resistivity-depth sections are most useful in conductive layered situations, but may be unreliable in areas of moderate to high resistivity where signal amplitudes are weak. In areas where in-phase responses have been suppressed by the effects of magnetite, the computed resistivities shown on the sections may be unreliable. The differential resistivity technique was developed by Dighem. It is more sensitive than the Sengpiel section to changes in the earth's resistivity and it reaches deeper.

¹ Sengpiel, K.P., 1988, Inverse Inversion of Airborne EM Data from Multilayered Ground: *Geophysical Prospecting* 36, 446-459.

² Huang, H. and Fraser, D.C., 1993, Differential Resistivity Method for Multi-frequency Airborne EM Sounding: presented at Intern. Airb. EM Workshop, Tucson, Ariz.

³ Constable et al, 1987, Occam's inversion: a practical algorithm for generating smooth models from electromagnetic sounding data: *Geophysics*, 52, 289-300.

Both the Occam and Multi-layer Inversions compute the layered earth resistivity model which would best match the measured EM data. The Occam inversion uses a series of thin, fixed layers (usually 20 x 5m and 10 x 10m layers) and computes resistivities to fit the EM data. The multi-layer inversion computes the resistivity and thickness for each of a defined number of layers (typically 3-5 layers) to best fit the data.

⁴ Huang H., and Palacky, G.J., 1991, Damped least-squares inversion of time domain airborne EM data based on singular value decomposition: *Geophysical Prospecting*, 39, 827-844.

4.0 CONCLUSIONS AND RECOMMENDATIONS

This report provides a description of the equipment, procedures and logistics of the survey. The digital data included with this report display the magnetic and conductive properties of the survey area.

It is recommended that image processing of existing geophysical data be considered, in order to extract the maximum amount of information from the survey results. Current software and imaging techniques often provide valuable information on structure and lithology, which may not be clearly evident on the contour and colour maps. These techniques can yield images which define subtle, but significant, structural details.

A complete assessment and evaluation of the survey data should be carried out by one or more qualified professionals who have access to, and can provide a meaningful compilation of, all available geophysical, geological and geochemical data.

Respectfully submitted,

FUGRO AIRBORNE SURVEYS

Michael J. Cain, P.Eng.
Geophysicist

APPENDIX A

LIST OF PERSONNEL

The following personnel were involved in the acquisition, processing, interpretation and presentation of data, of the RESOLVE airborne geophysical survey carried out for the United States Geological Survey over the Seco Creek area, Texas.

David Miles	Manager, Helicopter Operations
Emily Farquhar	Manager, Data Processing
Brett Robinson	Field Geophysicist
Will Marr	Geophysical Operator
Luke Kukovica	Pilot
Michael Cain	Project Geophysicist
Russell Imrie	Geophysical Data Processor
Lyn Vanderstarren	Drafting Supervisor
Albina Tonello	Secretary/Expeditor

All personnel are employees of Fugro Airborne Surveys, except for the pilot who is an employee of Questral Helicopters.

APPENDIX B

ARCHIVE DESCRIPTION

This CD-ROM contains final data archives of an airborne survey conducted by Fugro Airborne Surveys on behalf of United States Geological Survey over the Seco Creek area, Texas. Total coverage of the survey blocks amounted to 953 miles (1534 kilometres) over 2 survey blocks and several lines following the creeks through the survey area. The survey was flown from May 21 to 27, 2002.

Fugro Airborne Surveys Job #6025

The archives contain three directories.

1. Line Data: Geosoft GDB database with archive description.
2. Grids: Grids in Geosoft GRD format for the following parameters:
 1. Magnetic total field (IGRF corrected)
 2. 5 coplanar resistivities
3. Report: A digital copy of the operations report

Projection Description:

Datum:	NAD27
Ellipsoid:	Clarke 1866
Projection:	UTM (Zone: 14)
Central Meridian:	99° West
False Northing:	0
False Easting:	500000
Scale Factor:	0.9996
WGS84 to Local Conversion:	Molodensky
X,Y,Z Datum Shifts:	8 -159 -175

EM PARAMETERS

orientation	FREQUENCY		COIL SPACING
	nominal	actual	
coplanar	400 Hz	386 Hz	7.9 m
coplanar	1 500 Hz	1 514 Hz	7.9 m
coaxial	3 300 Hz	3 315 Hz	9.0 m
coplanar	6 200 Hz	6 122 Hz	7.9 m
coplanar	25 000 Hz	25 960 Hz	7.9 m
coplanar	100 000 Hz	106 400 Hz	7.9 m

DATABASE : 6025_Seco.GDB

=====

NUMBER OF DATABASE CHANNELS : 146

=====

1 - LINE	DBS-INC	0.10	LINE NUMBER
2 - FLIGHT	DBS-INC	0.10	FLIGHT NUMBER
3 - DATE	DBS-INC	0.10	FLIGHT DATE
4 - FID	DBS-INC	0.10	FIDUCIAL COUNTER
5 - UTC	DBS-INC	0.10	UTC TIME
6 - ALTBIRD	DBS-INC	0.10	BIRD RADAR ALTIMETER (METRES)
7 - ALTBIRD	DBS-INC	0.10	BIRD RADAR ALTIMETER RAW (METRES)
8 - ALTLASER	DBS-INC	0.10	BIRD LASER ALTIMETER PROCESSED (METRES)
9 - ALTRFT	DBS-INC	0.10	HELICOPTER RADAR ALTIMETER RAW (FEET)
10 - BALT	DBS-INC	0.10	BAROMETRIC ALTIMETER RAW (METRES)
11 - ALTBARO	DBS-INC	0.10	BAROMETRIC ALTIMETER PROCESSED (METRES)
12 - CPI100K	DBS-INC	0.10	COPLANAR INPHASE FULLY PROCESSED 100K HZ
13 - CPI1500	DBS-INC	0.10	COPLANAR INPHASE FULLY PROCESSED 1500 HZ
14 - CPI25K	DBS-INC	0.10	COPLANAR INPHASE FULLY PROCESSED 25K HZ
15 - CPI400	DBS-INC	0.10	COPLANAR INPHASE FULLY PROCESSED 400 HZ
16 - CPI6200	DBS-INC	0.10	COPLANAR INPHASE FULLY PROCESSED 6200 HZ
17 - CPIR100K	DBS-INC	0.10	COPLANAR INPHASE FILTERED 100K HZ
18 - CPIR1500	DBS-INC	0.10	COPLANAR INPHASE FILTERED 1500 HZ
19 - CPIR25K	DBS-INC	0.10	COPLANAR INPHASE FILTERED 25K HZ
20 - CPIR400	DBS-INC	0.10	COPLANAR INPHASE FILTERED 400 HZ
21 - CPIR6200	DBS-INC	0.10	COPLANAR INPHASE FILTERED 6200 HZ
22 - CPPL	DBS-INC	0.10	COPLANAR POWERLINE MONITOR
23 - CPPLR	DBS-INC	0.10	COPLANAR POWERLINE MONITOR RAW
24 - CPQ100K	DBS-INC	0.10	COPLANAR QUADRATURE FULLY PROCESSED 100K HZ
25 - CPQ1500	DBS-INC	0.10	COPLANAR QUADRATURE FULLY PROCESSED 1500 HZ
26 - CPQ25K	DBS-INC	0.10	COPLANAR QUADRATURE FULLY PROCESSED 25K HZ
27 - CPQ400	DBS-INC	0.10	COPLANAR QUADRATURE FULLY PROCESSED 400 HZ
28 - CPQ6200	DBS-INC	0.10	COPLANAR QUADRATURE FULLY PROCESSED 6200 HZ
29 - CPQR100K	DBS-INC	0.10	COPLANAR QUADRATURE FILTERED 100K HZ
30 - CPQR1500	DBS-INC	0.10	COPLANAR QUADRATURE FILTERED 1500 HZ
31 - CPQR25K	DBS-INC	0.10	COPLANAR QUADRATURE FILTERED 25K HZ
32 - CPQR400	DBS-INC	0.10	COPLANAR QUADRATURE FILTERED 400 HZ
33 - CPQR6200	DBS-INC	0.10	COPLANAR QUADRATURE FILTERED 6200 HZ
34 - CPSP	DBS-INC	0.10	COPLANAR SPHERICS MONITOR
35 - CPSPR	DBS-INC	0.10	COPLANAR SPHERICS MONITOR RAW
36 - CXI3300	DBS-INC	0.10	COAXIAL INPHASE FULLY PROCESSED 3300 HZ
37 - CXIR3300	DBS-INC	0.10	COAXIAL INPHASE FILTERED 3300 HZ
38 - CXPL	DBS-INC	0.10	COAXIAL POWERLINE MONITOR
39 - CXPLR	DBS-INC	0.10	COAXIAL POWERLINE MONITOR RAW
40 - CXQ3300	DBS-INC	0.10	COAXIAL QUADRATURE FULLY PROCESSED 3300 HZ
41 - CXQR3300	DBS-INC	0.10	COAXIAL QUADRATURE FILTERED 3300 HZ
42 - CXSP	DBS-INC	0.10	COAXIAL SPHERICS MONITOR
43 - CXSPR	DBS-INC	0.10	COAXIAL SPHERICS MONITOR RAW
44 - DTMB	DBS-INC	0.10	DIGITAL ELEVATION MODEL FROM BARO
45 - DTMBARO	DBS-INC	0.10	PROCESSED DIGITAL ELEVATION MODEL FROM BARO
46 - DTMGPSZ	DBS-INC	0.10	DIGITAL ELEVATION MODEL FROM GPSZ
47 - DTMZ	DBS-INC	0.10	PROCESSED DIGITAL ELEVATION MODEL FROM GPSZ
48 - DEP100K	DBS-INC	0.10	DEPTH 100K HZ FILTERED
49 - DEP1500	DBS-INC	0.10	DEPTH 1500HZ FILTERED
50 - DEP25K	DBS-INC	0.10	DEPTH 25K HZ FILTERED
51 - DEP3300	DBS-INC	0.10	DEPTH 3300 HZ FILTERED
52 - DEP400	DBS-INC	0.10	DEPTH 400 HZ FILTERED
53 - DEP6200	DBS-INC	0.10	DEPTH 6200 HZ FILTERED
54 - DEP100K_NF	DBS-INC	0.10	DEPTH 100K HZ NOT FILTERED
55 - DEP1500_NF	DBS-INC	0.10	DEPTH 1500HZ NOT FILTERED
56 - DEP25K_NF	DBS-INC	0.10	DEPTH 25K HZ NOT FILTERED
57 - DEP3300_NF	DBS-INC	0.10	DEPTH 3300 HZ NOT FILTERED
58 - DEP400_NF	DBS-INC	0.10	DEPTH 400 HZ NOT FILTERED
59 - DEP6200_NF	DBS-INC	0.10	DEPTH 6200 HZ NOT FILTERED

60 - DDEP100K	DBS-INC	0.10	DIFFERENTIAL DEPTH 100K HZ FILTERED
61 - DDEP1500	DBS-INC	0.10	DIFFERENTIAL DEPTH 1500HZ FILTERED
62 - DDEP25K	DBS-INC	0.10	DIFFERENTIAL DEPTH 25K HZ FILTERED
63 - DDEP400	DBS-INC	0.10	DIFFERENTIAL DEPTH 400 HZ FILTERED
64 - DDEP6200	DBS-INC	0.10	DIFFERENTIAL DEPTH 6200 HZ FILTERED
65 - DDEP100K_NF	DBS-INC	0.10	DIFFERENTIAL DEPTH 100K HZ NOT FILTERED
66 - DDEP1500_NF	DBS-INC	0.10	DIFFERENTIAL DEPTH 1500HZ NOT FILTERED
67 - DDEP25K_NF	DBS-INC	0.10	DIFFERENTIAL DEPTH 25K HZ NOT FILTERED
68 - DDEP400_NF	DBS-INC	0.10	DIFFERENTIAL DEPTH 400 HZ NOT FILTERED
69 - DDEP6200_NF	DBS-INC	0.10	DIFFERENTIAL DEPTH 6200 HZ NOT FILTERED
70 - CEN100K	DBS-INC	0.10	CENTROID DEPTH 100K HZ FILTERED
71 - CEN1500	DBS-INC	0.10	CENTROID DEPTH 1500HZ FILTERED
72 - CEN25K	DBS-INC	0.10	CENTROID DEPTH 25K HZ FILTERED
73 - CEN400	DBS-INC	0.10	CENTROID DEPTH 400 HZ FILTERED
74 - CEN6200	DBS-INC	0.10	CENTROID DEPTH 6200 HZ FILTERED
75 - CEN100K_NF	DBS-INC	0.10	CENTROID DEPTH 100K HZ NOT FILTERED
76 - CEN1500_NF	DBS-INC	0.10	CENTROID DEPTH 1500HZ NOT FILTERED
77 - CEN25K_NF	DBS-INC	0.10	CENTROID DEPTH 25K HZ NOT FILTERED
78 - CEN400_NF	DBS-INC	0.10	CENTROID DEPTH 400 HZ NOT FILTERED
79 - CEN6200_NF	DBS-INC	0.10	CENTROID DEPTH 6200 HZ NOT FILTERED
80 - DIURNAL	DBS-INC	0.10	DIURNAL CORRECTION APPLIED
81 - KPA1	DBS-INC	0.10	PRESSURE IN MBAR
82 - L100I	DBS-INC	0.10	BASE LEVELED INPHASE 100K HZ
83 - L100Q	DBS-INC	0.10	BASE LEVELED QUADRATURE 100K HZ
84 - L1K5I	DBS-INC	0.10	BASE LEVELED INPHASE 1500 HZ
85 - L1K5Q	DBS-INC	0.10	BASE LEVELED QUADRATURE 1500 HZ
86 - L1K7I	DBS-INC	0.10	BASE LEVELED INPHASE 3300 HZ
87 - L1K7Q	DBS-INC	0.10	BASE LEVELED QUADRATURE 3300 HZ
88 - L25KI	DBS-INC	0.10	BASE LEVELED INPHASE 25K HZ
89 - L25KQ	DBS-INC	0.10	BASE LEVELED QUADRATURE 25K HZ
90 - L400I	DBS-INC	0.10	BASE LEVELED INPHASE 400 HZ
91 - L400Q	DBS-INC	0.10	BASE LEVELED QUADRATURE 400 HZ
92 - L6K2I	DBS-INC	0.10	BASE LEVELED INPHASE 6200 HZ
93 - L6K2Q	DBS-INC	0.10	BASE LEVELED QUADRATURE 6200 HZ
94 - LAT_BIRD	DBS-INC	0.10	LATITUDE BIRD GPS WGS84 (NAD83)
95 - LAT_HELI	DBS-INC	0.10	LATITUDE HELI GPS WGS84 (NAD83)
96 - LAT4	DBS-INC	0.10	LATITUDE HELI GPS UNPROCESSED WGS84 (NAD83)
97 - LON_BIRD	DBS-INC	0.10	LONGITUDE BIRD GPS WGS84 (NAD83)
98 - LON_HELI	DBS-INC	0.10	LONGITUDE HELI GPS WGS84 (NAD83)
99 - LON4	DBS-INC	0.10	LONGITUDE HELI GPS UNPROCESSED WGS84 (NAD83)
100 - LSR1	DBS-INC	0.10	RAW LASER ALTIMETER, NO CONVERSION FACTOR
101 - MAG	DBS-INC	0.10	FINAL TOTAL MAGNETIC FIELD IGRF REMOVED
102 - MAGD	DBS-INC	0.10	DIURNAL CORRECTED TOTAL MAGNETIC FIELD
103 - IGRF	DBS-INC	0.10	IGRF
104 - MAGSP	DBS-INC	0.10	TOTAL MAGNETIC FIELD DESPIKED
105 - MAGUR	DBS-INC	0.10	RAW TOTAL MAGNETIC FIELD
106 - RES100K	DBS-INC	0.10	RESISTIVITY 100K HZ FILTERED
107 - RES1500	DBS-INC	0.10	RESISTIVITY 1500 HZ FILTERED
108 - RES25K	DBS-INC	0.10	RESISTIVITY 25K HZ FILTERED
109 - RES3300	DBS-INC	0.10	RESISTIVITY 3300 HZ FILTERED
110 - RES400	DBS-INC	0.10	RESISTIVITY 400 HZ FILTERED
111 - RES6200	DBS-INC	0.10	RESISTIVITY 6200 HZ FILTERED
112 - RES100K_NF	DBS-INC	0.10	RESISTIVITY 100K HZ NOT FILTERED
113 - RES1500_NF	DBS-INC	0.10	RESISTIVITY 1500 HZ NOT FILTERED
114 - RES25K_NF	DBS-INC	0.10	RESISTIVITY 25K HZ NOT FILTERED
115 - RES3300_NF	DBS-INC	0.10	RESISTIVITY 3300 HZ NOT FILTERED
116 - RES400_NF	DBS-INC	0.10	RESISTIVITY 400 HZ NOT FILTERED
117 - RES6200_NF	DBS-INC	0.10	RESISTIVITY 6200 HZ NOT FILTERED
118 - DRES100K	DBS-INC	0.10	DIFFERENTIAL RESISTIVITY 100K HZ FILTERED
119 - DRES1500	DBS-INC	0.10	DIFFERENTIAL RESISTIVITY 1500 HZ FILTERED
120 - DRES25K	DBS-INC	0.10	DIFFERENTIAL RESISTIVITY 25K HZ FILTERED
121 - DRES400	DBS-INC	0.10	DIFFERENTIAL RESISTIVITY 400 HZ FILTERED
122 - DRES6200	DBS-INC	0.10	DIFFERENTIAL RESISTIVITY 6200 HZ FILTERED
123 - DRES100K_NF	DBS-INC	0.10	DIFFERENTIAL RESISTIVITY 100K HZ NOT FILTERED
124 - DRES1500_NF	DBS-INC	0.10	DIFFERENTIAL RESISTIVITY 1500 HZ NOT FILTERED
125 - DRES25K_NF	DBS-INC	0.10	DIFFERENTIAL RESISTIVITY 25K HZ NOT FILTERED
126 - DRES400_NF	DBS-INC	0.10	DIFFERENTIAL RESISTIVITY 400 HZ NOT FILTERED
127 - DRES6200_NF	DBS-INC	0.10	DIFFERENTIAL RESISTIVITY 6200 HZ NOT FILTERED
128 - X	DBS-INC	0.10	FINAL BIRD UTM X CLARK 1866 (NAD27)
129 - X_HELI	DBS-INC	0.10	UTM X FROM HELI GPS CLARK 1866 (NAD27)
130 - Y	DBS-INC	0.10	FINAL UTM Y CLARK 1866 (NAD27)
131 - Y_HELI	DBS-INC	0.10	UTM Y FROM HELI GPS CLARK 1866 (NAD27)
132 - Z_B	DBS-INC	0.10	FINAL Z
133 - Z_H	DBS-INC	0.10	Z FROM HELI GPS
134 - GPSZ4	DBS-INC	0.10	Z FROM HELI GPS RAW
135 - _100I	DBS-INC	0.10	RAW INPHASE 100K HZ
136 - _100Q	DBS-INC	0.10	RAW QUADRATURE 100K HZ
137 - _1K5I	DBS-INC	0.10	RAW INPHASE 1500 HZ

138	-	_1K5Q	DBS-INC	0.10	RAW QUADRATURE 1500 HZ
139	-	_1K7I	DBS-INC	0.10	RAW INPHASE 3300 HZ
140	-	_1K7Q	DBS-INC	0.10	RAW QUADRATURE 3300 HZ
141	-	_25KI	DBS-INC	0.10	RAW INPHASE 25K HZ
142	-	_25KQ	DBS-INC	0.10	RAW QUADRATURE 25K HZ
143	-	_400I	DBS-INC	0.10	RAW INPHASE 400 HZ
144	-	_400Q	DBS-INC	0.10	RAW QUADRATURE 400 HZ
145	-	_6K2I	DBS-INC	0.10	RAW INPHASE 6200 HZ
146	-	_6K2Q	DBS-INC	0.10	RAW QUADRATURE 6200 HZ

=====

APPENDIX C

PROCESSING LOG

Electromagnetics Processing:

All steps performed on all EM channels unless otherwise stated.

- Due to a conversion error in the transfer of the raw helicopter data file to the field database, the coaxial 3300 Hz data required a multiplier of 2. This factor was applied to the coaxial in-phase and quadrature channels prior to delivery of the final archives but would not have been applied to any of the preliminary data products.
- Filter raw EM channels 11pt median followed by 11 pt Hanning
L400I → CPIR400, L400Q → CPQR400
L1K5I → CPIR1500, L1K5Q → CPQR1500
L1K7I → CXIR3300, L1K7Q → CXQR3300
L6K2I → CPIR6200, L6K2IQ → CPQR6200
L25KI → CPIR25K, L25KQ → CPQR25K
L100I → CPIR100K, L100Q → CPQR100K
- Apply manual leveling picks to filtered EM channels.
- Gain adjustment for 100 kHz and 25 kHz to correct known errors from EM calibration. Gain increase of 18% and 13% applied to the inphase and quadrature of the 100 kHz and 25 kHz respectively. These gain corrections would not have been applied to any preliminary data products.
- Calculate resistivity and depth channels with Fugro proprietary software using filtered and gained EM data.
- Calculate centroid depths (CEN*), differential resistivity (DRES*) and differential depths (DRES*).
- Filter output channels (RES*, DEP*, DRES*, DDEP*, CEN*). 21pt median 21pt Hanning. All unfiltered channels are in the archive with the suffix _NF.
- See the archive CD-ROM or Appendix B for complete channel name description.

Magnetics Processing (from Russell Imrie)

MAGSP is the raw channel MAGUR manually despiked using a fourth difference as a reference. All spikes occurred in areas where the mag was smoothly varying. This allowed the defaulted areas to be interpolated using an Akima spline. A 5 point hanning was used to smooth the transition from areas defaulted and splined to areas not defaulted. A lag of 11 scans (1.1 seconds) was applied to the mag. DIURNAL data were examined for spikes and applied to produce the MAGDL channel. MAGDL and MAGL were gridded and compared to ensure no valid anomalies were being removed and that the grid was improved by the diurnal application.

IGRF was computed on a point by point basis using the final Z channel as height above sea level and a year 2000 table of coefficients. May 2002 was the calculation date. Tie line leveling was not used as the altitude and gradient misties were too great. A grid based vertical gradient was calculated from the IGRF corrected mag. It was shadowed and inspected but revealed no leveling errors on either area.

Digital Elevation Model Processing (from Russell Imrie)

The barometric altimeter was converted to metres and filtered with an 11 point Hanning. It was profiled and inspected against the Z channel for spikes. Significant steps were removed and splined or DC shifted to match the character of the Z trace. The Z data were also inspected in this manner, compared to the filtered barometric altimeter trace for sharp changes. Corrections were made by defaulting and splining or by shifting data so the Z profile matched the character of the Baro. Altbirdr has been filtered by Mike Cain to produce ALTBIRD. ALTBIRD had a couple of spikes that were removed and splined. ALTLASER was produced by Mike Cain and severe spikes were removed and splined using ALTBIRD as a reference. Some of the ALTLASER data spikes covered areas where the ALTBIRD showed rapid variation. These were not splined.

DTM's were calculated as follows:
DTMB - BALT-ALTBIRD
DTMZ - Z-ALTBIRD

These were contoured, inspected and compared. The tie line leveling corrections were applied to the BALT channel to produce the final BALT channel.

APPENDIX D

BACKGROUND INFORMATION

D.1 Resistivity Mapping

Areas of widespread conductivity are commonly encountered during surveys. These conductive zones may reflect alteration zones, shallow-dipping sulphide or graphite-rich units, saline pools or water tables, or conductive overburden. In such areas, anomalies can be generated by decreases of only 5 m in survey altitude as well as by increases in conductivity. The typical flight record in conductive areas is characterized by in-phase and quadrature channels which are continuously active. Local EM peaks reflect either increases in conductivity of the earth or decreases in survey altitude. For such conductive areas, apparent resistivity profiles and contour maps are necessary for the correct interpretation of the airborne data. The advantage of the resistivity parameter is that anomalies caused by minor altitude changes are virtually eliminated, so the resistivity data reflect only those anomalies caused by conductivity changes. The resistivity analysis also helps the interpreter to differentiate between conductive bedrock and conductive overburden. For example, discrete conductors will generally appear as narrow lows on the contour map and broad conductors (e.g., overburden, tailings ponds leaks or saline water tables) will appear as wide lows.

The apparent resistivity is calculated using the pseudo-layer (or buried) half-space model defined by Fraser (1978)⁵. This model consists of a resistive layer overlying a conductive half-space. The depth channels give the apparent depth below surface of the conductive material. The apparent depth is simply the apparent thickness of the overlying resistive layer. The apparent depth (or thickness) parameter will be positive when the upper layer is more resistive than the underlying material, in which case the apparent depth may be quite close to the true depth.

The apparent depth will be negative when the upper layer is more conductive than the underlying material, and will be zero when a homogeneous half-space exists. The apparent depth parameter must be interpreted cautiously because it will contain any errors which may exist in the measured altitude of the EM bird (e.g., as caused by a dense tree cover). The inputs to the conductivity algorithm are the in-phase and quadrature components of the coplanar coil-pair. The outputs are the apparent conductivity of the conductive half-space (the source) and the sensor-source distance. The flying height is not an input variable, and the output conductivity and sensor-source distance are independent of the flying height when the conductivity of the measured material is sufficient to yield significant in-phase as well as quadrature responses. The apparent depth, discussed above, is simply the sensor-source distance minus the

⁵ Resistivity mapping with an airborne multicoil electromagnetic system: Geophysics, v. 43, p.144-172

measured altitude or flying height. Consequently, errors in the measured altitude will affect the apparent depth parameter but not the apparent conductivity parameter.

The apparent depth parameter is a useful indicator of simple layering in areas lacking a heavy tree cover. The DIGHEM system has been flown for purposes of permafrost mapping, where positive apparent depths were used as a measure of permafrost thickness. However, little quantitative use has been made of negative apparent depths because the absolute value of the negative depth is not a measure of the thickness of the conductive upper layer and, therefore, is not meaningful physically. Qualitatively, a negative apparent depth estimate usually shows that the EM anomaly is caused by a conductive layer at surface. Consequently, the apparent depth channel can be of significant help in distinguishing between overburden and bedrock conductors.

The DP channels, which give the apparent depth to the conductive material, also help to determine whether a conductive response arises from surficial material or from a conductive zone in the bedrock. When these channels ride above the zero level on the digital profiles (i.e., depth is negative), it implies that the EM and conductivity profiles are responding primarily to a conductive upper layer, i.e., conductive overburden. If the DP channels are below the zero level, it indicates that a resistive upper layer exists, and this usually implies the existence of a bedrock conductor. If the low frequency DP channel is below the zero level and the high frequency DP is above, this suggests that a bedrock conductor occurs beneath conductive cover.

D.2 Reduction of Geologic Noise

Geologic noise refers to unwanted geophysical responses. For purposes of airborne EM surveying, geologic noise refers to EM responses caused by conductive overburden and magnetic permeability.

Magnetite produces a form of geological noise on the in-phase channels of all EM systems. Rocks containing less than 1 % magnetite can yield negative in-phase anomalies caused by magnetic permeability. When magnetite is widely distributed throughout a survey area, the in-phase EM channels may continuously rise and fall, reflecting variations in the magnetite percentage, flying height, and overburden thickness. This can lead to difficulties in recognizing deeply buried bedrock conductors, particularly if conductive overburden also exists.

D.3 Magnetics

Total field magnetics provides information on the magnetic properties of the earth materials in the survey area. The information can be used to locate magnetic bodies of direct interest for exploration, and for structural and lithological mapping.

The total field magnetic response reflects the abundance of magnetic material, in the source. Magnetite is the most common magnetic mineral. Other minerals such as ilmenite, pyrrhotite, franklinite, chromite, hematite, arsenopyrite, limonite and pyrite are also magnetic, but to a lesser extent than magnetite on average.

In some geological environments, an EM anomaly with magnetic correlation has a greater likelihood of being produced by sulphides than one which is non-magnetic. However, sulphide ore bodies may be non-magnetic (e.g., the Kidd Creek deposit near Timmins, Canada) as well as magnetic (e.g., the Mattabi deposit near Sturgeon Lake, Canada).

Iron ore deposits will be anomalously magnetic in comparison to surrounding rock due to the concentration of iron minerals such as magnetite, ilmenite and hematite.

Changes in magnetic susceptibility often allow rock units to be differentiated based on the total field magnetic response. Geophysical classifications may differ from geological classifications if various magnetite levels exist within one general geological classification. Geometric considerations of the source such as shape, dip and depth, inclination of the earth's field and remanent magnetization will complicate such an analysis.

In general, mafic lithologies contain more magnetite and are therefore more magnetic than many sediments which tend to be weakly magnetic. Metamorphism and alteration can also increase or decrease the magnetization of a rock unit.

Textural differences on a total field magnetic contour, colour or shadow map, due to the frequency of activity of the magnetic parameter resulting from inhomogeneities in the distribution of magnetite within the rock, may define certain lithologies. For example, near surface volcanics may display highly complex contour patterns with little line-to-line correlation.

Rock units may be differentiated based on the plan shapes of their total field magnetic responses. Mafic intrusive plugs can appear as isolated "bulls-eye" anomalies. Granitic intrusives appear as sub-circular zones, and may have contrasting rings due to contact metamorphism. Generally, granitic terrain will lack a pronounced strike direction, although granite gneiss may display strike.

Linear north-south units are theoretically not well-defined on total field magnetic maps in equatorial regions due to the low inclination of the earth's magnetic field. However, most stratigraphic units will have variations in composition along strike which will cause the units to appear as a series of alternating magnetic highs and lows.

Faults and shear zones may be characterized by alteration which causes destruction of magnetite (e.g., weathering) which produces a contrast with surrounding rock. Structural breaks may be filled by magnetite-rich, fracture filling material as is the case with diabase dikes, or by non-magnetic felsic material.

Faulting can also be identified by patterns in the magnetic total field contours or colours. Faults and dikes tend to appear as lineaments and often have strike lengths of several kilometres. Offsets in narrow, magnetic, stratigraphic trends also delineate structure. Sharp contrasts in magnetic lithologies may arise due to large displacements along strike-slip or dip-slip faults.

APPENDIX E

FLIGHT LOGS (IN USGS FILES)

APPENDIX F

TESTS AND CALIBRATIONS

EM Calibrations

CALIBRATION OF THE DIGHEM DIGITAL (DSP) SYSTEM

The calibration method used in the digital Dighem^V has been developed as a significant improvement over the practices described by Fitterman (1998), which practices were originally developed through experimentation and consultation between Fugro and the United States Geological Survey. The problems defined by Fitterman, including jig calibration and conductive ground response, are obviated by calibration at high altitude using internal, rigidly mounted, automatically triggered and measured calibration coils.

Calibration of the system during the survey will use the Fugro AutoCal™ automatic, internal calibration process. At the beginning and end of each flight, and at intervals during the flight, the system will be flown up to high altitude to remove it from any “ground effect” (response from the earth). Any remaining signal from the receiver coils (base level) will be measured as the zero level, and removed from the data collected until the time of the next calibration. Following the zero level setting, internal calibration coils, for which the response phase and amplitude have been determined at the factory, are automatically triggered – one for each frequency. The on-time of the coils is sufficient to determine an accurate response through any ambient noise. The receiver response to each calibration coil “event” is compared to the expected response (from the factory calibration) for both phase angle and amplitude, and the applied phase and gain corrections adjusted to bring the data to the correct value.

In addition, the output of the transmitter coils are continuously monitored during the survey, and the applied gains adjusted to correct for any change in transmitter output (due to heating, etc.)

Because the internal calibration coils are calibrated at the factory (on a resistive halfspace) ground calibrations using external calibration coils on-site are not necessary for system calibration. A check calibration may be carried out on-site to ensure all systems are working correctly. All system calibrations will be carried out in the air, at sufficient altitude that there will be no measurable response from the ground.

The internal calibration coils are rigidly positioned and mounted in the system relative to the transmitter and receiver coils. In addition, when the internal calibration coils are calibrated at the factory, a rigid jig is employed to ensure accurate response from the external coils.

Using real time Fast Fourier Transforms and the calibration procedures outlined above, the data will be processed in real time from measured total field at a high sampling rate to in-phase and quadrature values at 10 samples per second.

Greg Hodges, Chief Geophysicist 01/04/09

References:

Fitterman, D.V., (1998). Sources of calibration errors in helicopter EM data. Exploration Geophysics 29, 65-70.

External Calibration Results

May 21, 2002 Start calibrations. In Seco Creek survey area

FREQUENCY	CHANNEL	INTERNAL		EXTERNAL		PHASE
		MEASURED	TARGET	MEASURED	TARGET	
400	L400I	207.0	200.0	208.0	200.4	-233.0
	L400Q	204.0	200.0	200.0	200.4	-9.0
1500	L1K5I	185.0	183.0	199.0	204.2	-175.0
	L1K5Q	180.0	183.0	189.0	204.2	6.0
3300	L1K7I	93.0	94.0	88.0	99.9	-259.0
	L1K7Q	92.0	94.0	89.0	99.9	-4.0
6200	L6K2I	830.0	822.0	186.0	207.5	-414.0
	L6K2Q	827.0	822.0	195.0	207.5	-10.0
25000	L25KI	404.0	409.0	132.0	192.5	-1695.0
	L25KQ	398.0	409.0	155.0	192.5	-76.0
100000	L100I	310.0	320.0	80.0	178.8	-4430.0
	L100Q	319.0	320.0	92.0	178.8	-322.0

May 27, 2002 End calibrations. In Seco Creek survey area

FREQUENCY	CHANNEL	INTERNAL		EXTERNAL		PHASE
		MEASURED	TARGET	MEASURED	TARGET	
400	L400I	206.0	200.0	210.0	200.4	-225.0
	L400Q	204.0	200.0	202.0	200.4	-9.0
1500	L1K5I	182.0	183.0	199.0	204.2	-261.0
	L1K5Q	180.0	183.0	192.0	204.2	3.0
3300	L1K7I	92.0	94.0	87.0	99.9	-273.0
	L1K7Q	94.0	94.0	88.0	99.9	-5.0
6200	L6K2I	824.0	822.0	187.0	207.5	-439.0
	L6K2Q	826.0	822.0	198.0	207.5	-12.0
25000	L25KI	402.0	409.0	131.0	192.5	-1661.0
	L25KQ	402.0	409.0	156.0	192.5	-60.0
100000	L100I	311.0	320.0	*	178.8	-3724.0
	L100Q	311.0	320.0	*	178.8	-201.0

* excessive noise could not determine data values

June 6, 2002 Mountsberg calibration site, Milton, Ontario

FREQUENCY	CHANNEL	INTERNAL		EXTERNAL		PHASE
		MEASURED	TARGET	MEASURED	TARGET	
400	L400I	203.0	200.0	209.2	200.4	-238.0
	L400Q	202.8	200.0	203.5	200.4	-12.0
1500	L1K5I	182.2	183.0	200.0	204.2	-250.0
	L1K5Q	181.9	183.0	193.0	204.2	3.5
3300	L1K7I	94.5	94.0	88.0	99.9	-222.0
	L1K7Q	93.9	94.0	88.0	99.9	-3.0
6200	L6K2I	825.0	822.0	189.3	207.5	-456.0
	L6K2Q	824.0	822.0	198.3	207.5	-7.0
25000	L25KI	419.8	409.0	142.3	192.5	-1950.0
	L25KQ	407.4	409.0	156.7	192.5	3.0
100000	L100I	316.3	320.0	79.0	178.8	-1479.0
	L100Q	321.0	320.0	80.0	178.8	16.0

Notes:

- Differences in the “measured” and “target” values in the external calibrations are corrected using scaling factors in the DSP software. The important numbers in the calibration tables above are the “measured” and “target” values in the internal calibrations. These offsets can also be monitored during flight using digital data from the “turns” in the database.
- No changes were made during these calibrations. The final calibration from Mountsberg on June 6 represents how the system was calibrated during the survey.

Helicopter Electromagnetic and Magnetic Survey Data and Maps, Seco Creek Area, Medina and Uvalde Counties, Texas

By Bruce D. Smith, David V. Smith, Patricia L. Hill, *and* Victor F. Labson

USGS Open File Report: 2003-226

NOTES

From the USGS Website: <http://pubs.usgs.gov/of/2003/ofr-03-226/> (accessed 11/24/2012)

Digital Data

[Contents TXT file \(4.KB\)](#) Listing of subdirectories and files.

[HP-Plots Directory](#)

The files contained in this subdirectory are plot files suitable for a large format Hewlett Packard Printer such as a 755cm.

[LineData Directory](#)

Flight line data given in an ASCII database.

[Reports Directory](#)

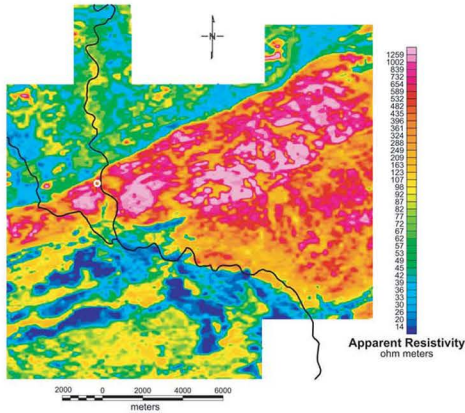
Contractors report of each channel description.

[Grids Directory](#)

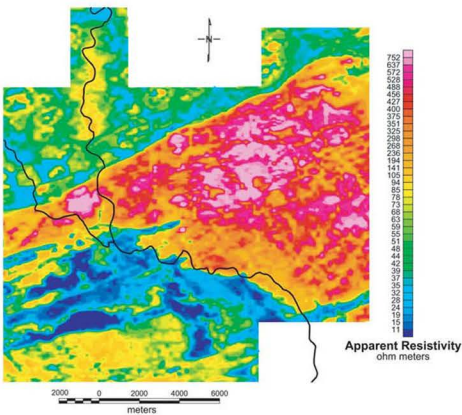
Grids of the magnetic field data and the apparent resistivities for the horizontal coplanar coil pairs.

[MapImages Directory](#)

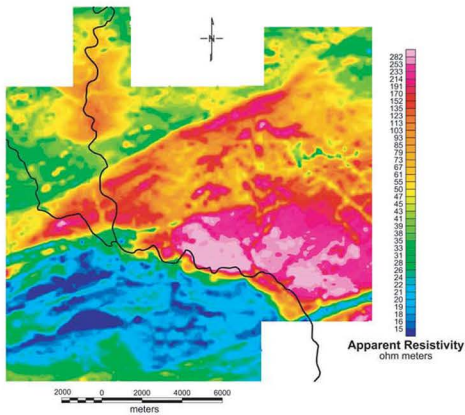
Contains geotiff (UTM projected tif files) of the grids.



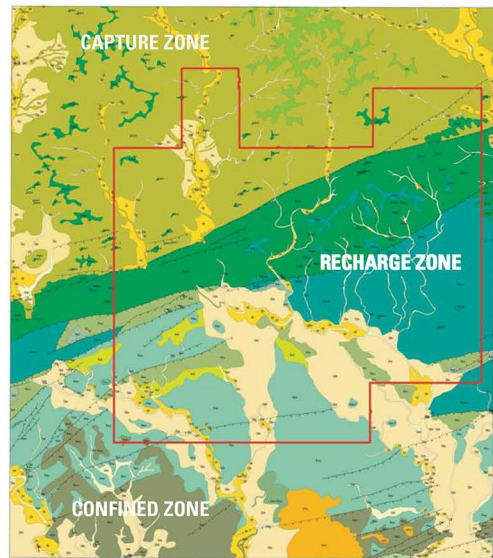
a. 100 KHz



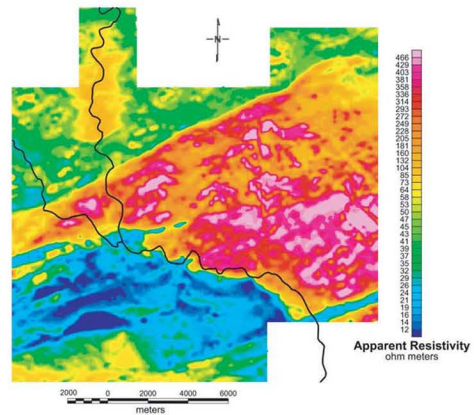
b. 25 KHz



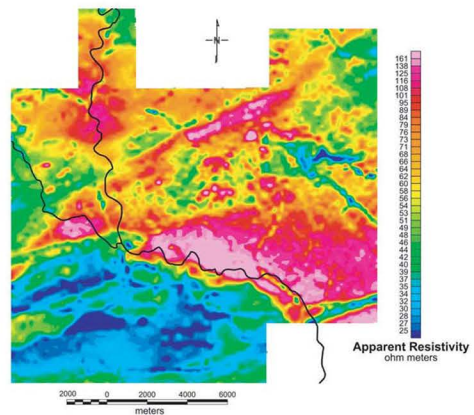
d. 1500 Hz



i. Geologic map (Kyle and Collins, 2003) of four 7.5' quadrangles (see text for lithologic units) that cover the study area shown by red box.



c. 6200 Hz



e. 400 Hz

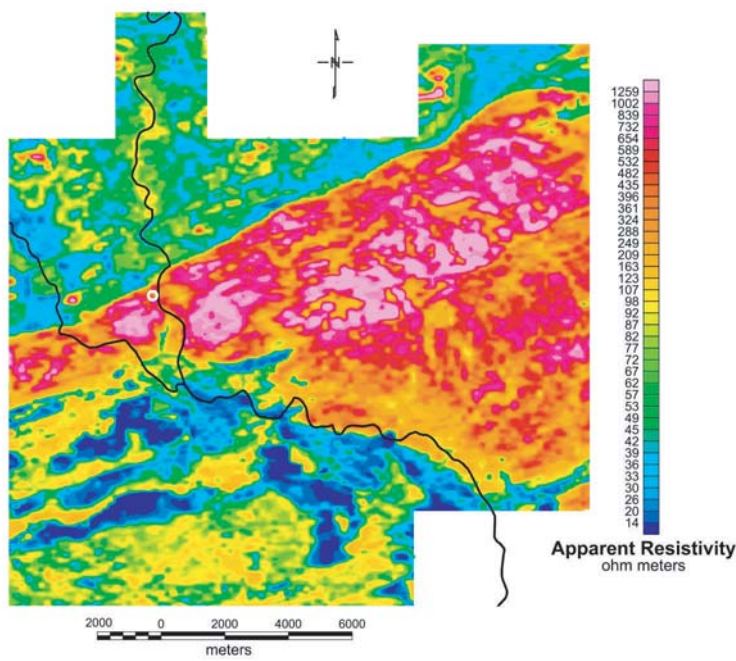
The red box in (i) shows the Seco Creek airborne geophysical survey area. The capture zone consists mostly of the Trinity Group with hills tops of Edwards Group. The recharge zone consists of the Upper and Lower Devils River formations of the Edwards Group. Exposures in the confined zone are formations younger than the Edwards. The Del Rio Clay caps the Edwards Group and accounts for much of the low apparent resistivity shown in the geophysical maps. Apparent resistivity maps have color scales that reflect maximum and minimum values for the indicated frequency. Thus particular color scales are unique to each map. Heavy wavy lines are the major drainages of Seco Creek and Little Seco Creek that occupy yellow Quaternary areas in (i). The circle shown in (a) is the approximate location of the Valdina Farms sinkhole. Decreasing frequency probes deeper with specific depth of investigation depending also on the resistivity of the subsurface. At the highest frequency (a), the exploration depth is only a few meters at most. The maximum exploration depth at the lowest frequency (e) in areas of higher resistivity (reds) is on the order of 100 meters.

GEOLOGIC AND APPARENT RESISTIVITY MAPS FOR THE SECO CREEK STUDY AREA

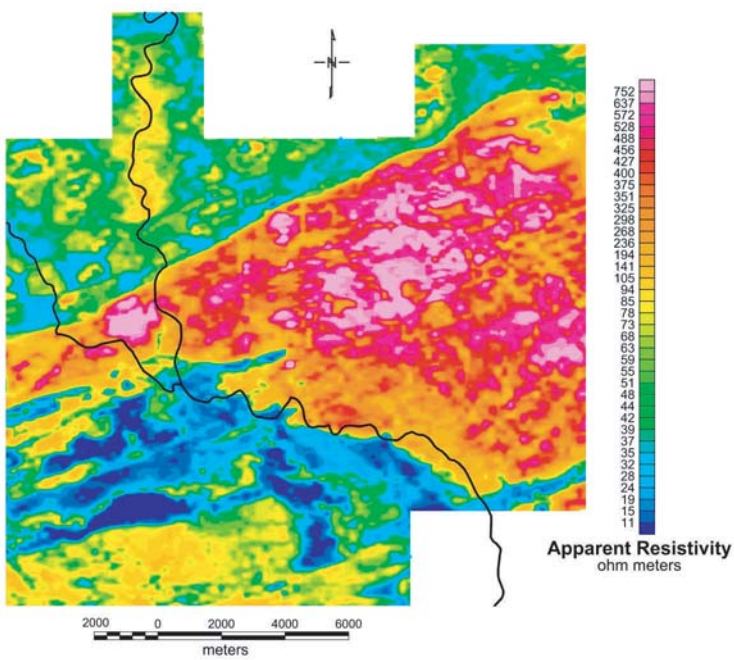
by
Bruce D. Smith, David V. Smith, Patricia L. Hill, and Victor F. Labson

Note: Large-format version of the plate for this report is available at:

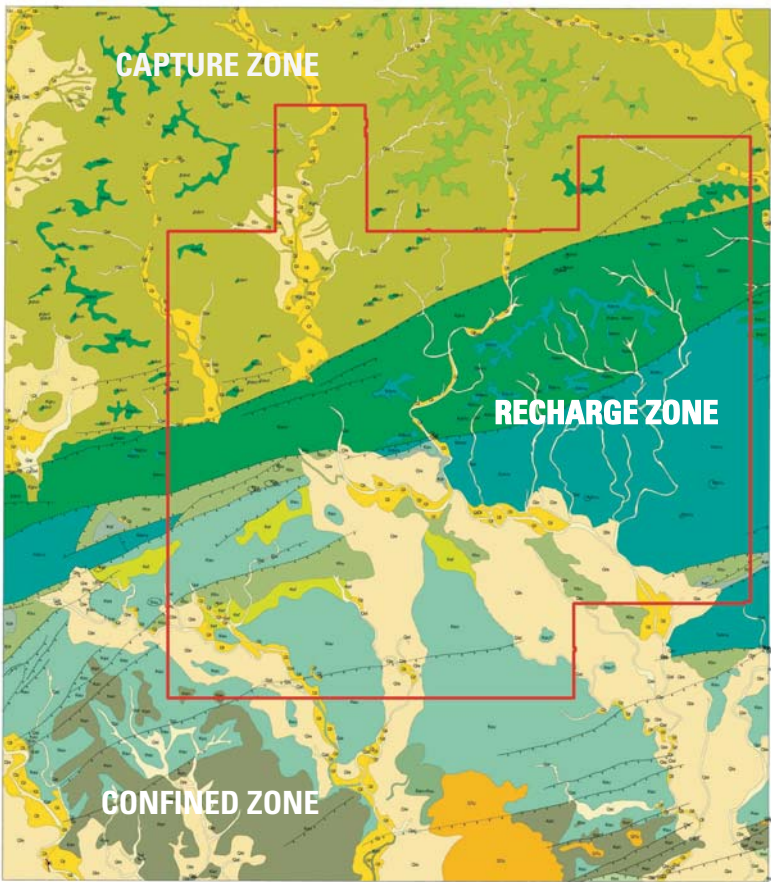
http://www.edwardsaquifer.org/documents/2003_Smith-et-al_HelicopterSurveySecoMedinaUvalde-Plate.pdf



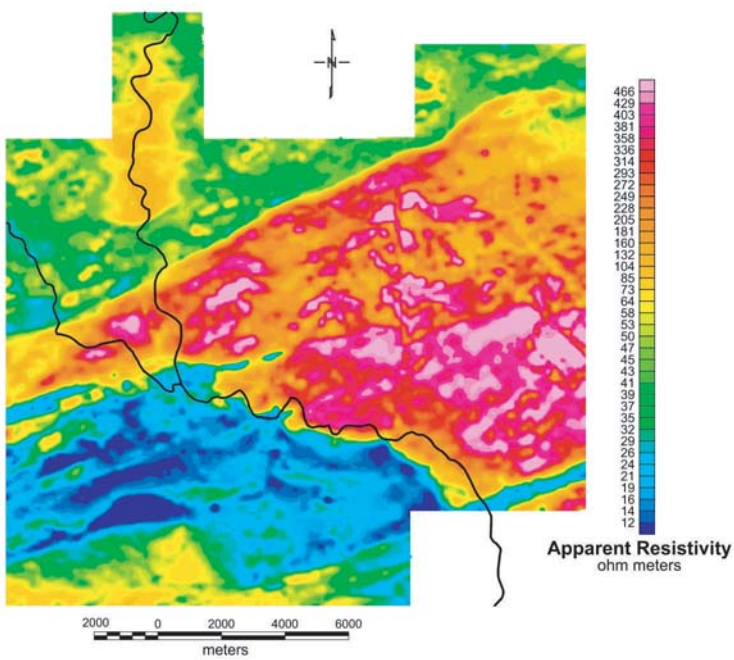
a. 100 KHz



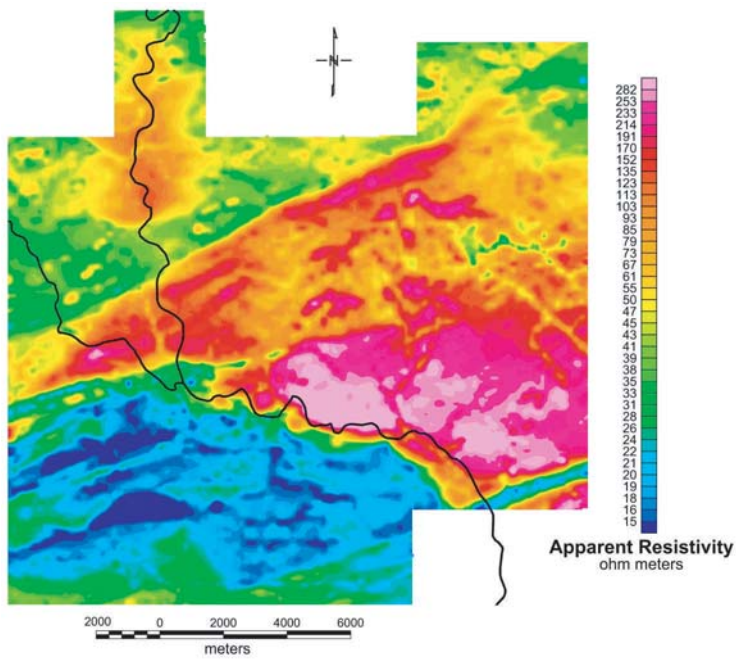
b. 25 KHz



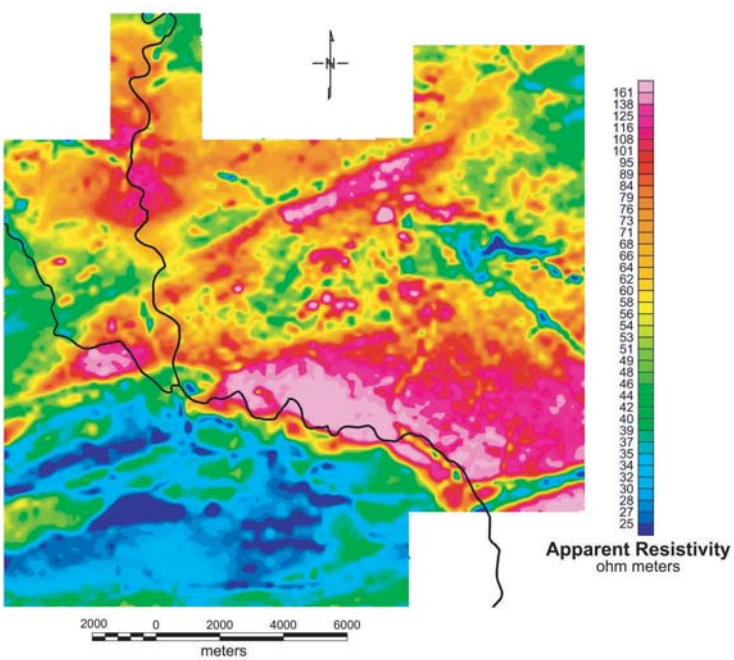
i. Geologic map (Kyle and Collins, 2003) of four 7.5' quadrangles (see text for lithologic units) that cover the study area shown by red box.



c. 6200 Hz



d. 1500 Hz



e. 400 Hz

The red box in (i) shows the Seco Creek airborne geophysical survey area. The capture zone consists mostly of the Trinity Group with hills tops of Edwards Group. The recharge zone consists of the Upper and Lower Devils River formations of the Edwards Group. Exposures in the confined zone are formations younger than the Edwards. The Del Rio Clay caps the Edwards Group and accounts for much of the low apparent resistivity shown in the geophysical maps. Apparent resistivity maps have color scales that reflect maximum and minimum values for the indicated frequency. Thus particular color scales are unique to each map. Heavy wavy lines are the major drainages of Seco Creek and Little Seco Creek that occupy yellow Quaternary areas in (i). The circle shown in (a) is the approximate location of the Valdina Farms sinkhole. Decreasing frequency probes deeper with specific depth of investigation depending also on the resistivity of the subsurface. At the highest frequency (a), the exploration depth is only a few meters at most. The maximum exploration depth at the lowest frequency (e) in areas of higher resistivity (reds) is on the order of 100 meters.

GEOLOGIC AND APPARENT RESISTIVITY MAPS FOR THE SECO CREEK STUDY AREA
by
Bruce D. Smith, David V. Smith, Patricia L. Hill, and Victor F. Labson